Comprehensive synthesis of monohydroxy-cucurbit[n]urils (n = 5, 6, 7, 8): High purity and high conversions

Ayhan, Mehmet M.; Karoui, Hakim; Hardy, Micael; Rockenbauer, Antal; Charles, Laurence; Rosas, Roselyne; Udachin, Konstantin; Tordo, Paul; Bardelang, David; Ouari, Olivier

National Research Council Canada   Conseil national de recherches Canada

Canada

Biexciton Binding of Dirac fermions Confined in Colloidal Graphene Quantum Dots

Cheng Sun,[†] Florian Figge,[†] Isil Ozfidan,[§] Marek Korkusinski,[‡] Xin Yan,[∥] Liang-shi Li,[∥] Pawel Hawrylak,*,[§] and John A. McGuire*,[†]

[†]Department of Physics and Astronomy, Michigan State University, East Lansing, Michigan 48824, United States

[‡]Quantum Theory Group, Security and Disruptive Technologies, Emerging Technologies Division, National Research Council of Canada, Ottawa, Ontario, K1A OR6 Canada

[§]Department of Physics, University of Ottawa, Ottawa, Ontario K1N 6N5, Canada

[∥]Department of Chemistry, Indiana University, Bloomington, Indiana 47405, United States

ABSTRACT: We present transient absorption measurements and microscopic theory of biexciton binding in triangular colloidal graphene quantum dots consisting of 168 sp^2-hybridized C atoms. We observe optical transitions from the lowest orbitally dark singlet exciton states to states below the energy of an unbound dark+bright singlet-exciton pair. Through microscopic calculations of the low-energy exciton and biexciton states via tight-binding, Hartree−Fock, and configuration interaction methods, the spectra reveal a biexciton consisting primarily of a dark-bright singlet-pair bound by ∼0.14 eV.

KEYWORDS: Graphene quantum dot, Dirac fermions, biexciton binding, transient absorption, Hartree−Fock, configuration interaction
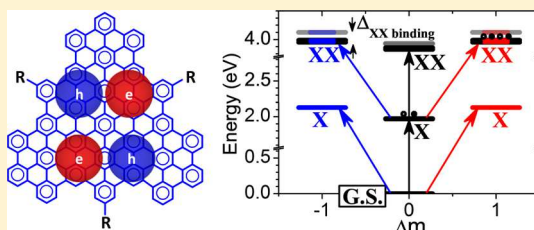
A central topic in nanoscience is the interactions between quasiparticles. In strongly confined nanoscale systems, these interactions are enhanced and lead to quantitatively and even qualitatively different phenomena than are observed in their bulk counterparts. These include enhanced biexciton binding,[1,2] rapid nonradiative Auger recombination,[3−5] and potentially efficient carrier multiplication.[6,7] At the heart of such phenomena are the enforced proximity of carriers and the large extent of the carrier wave functions in momentum space, which reduces constraints associated with conservation of crystal momentum.[8,9] In the context of biexcitons, graphene quantum dots are especially interesting, since screening is much weaker in a two-dimensional lattice of light atoms than a three-dimensional crystal of heavy atoms such as Cd and Se that feature so prominently in semiconductor quantum dot systems. Only recently, though, have graphene quantum dots been synthesized by bottom-up techniques[10,11] in sizes large enough that the lowest confinement-induced electron and hole states can be understood in terms of confined Dirac fermions.[12,13] This offers opportunities for new insights into interactions between Dirac fermions and applications in nanotechnology.

In graphene, understanding interactions of Dirac fermions and the nature of the possible ground states remains challenging.[14−27] Unlike in metals where the ratio of the Coulomb energy to the kinetic energy is proportional to the average distance between electrons, r_s, in graphene this ratio is independent of density and proportional to $(v_F \kappa)^{-1}$ where v_F is the Fermi velocity and κ is the dielectric constant.[15] Several theoretical predictions include insulating ground states[15,24,27]

and excitonic instabilities.[15,23,25,26] However, many experimental properties can be explained based on a noninteracting model of Dirac fermions;[14] electron−electron (e−e) interactions appear to lead only to renormalization of the Fermi velocity[17−19,21,22] of Dirac fermions consistent with weak e−e interactions in a semimetallic state.[16] In contrast, there are few experimental reports of excitonic signatures in graphene,[20,28] particularly with regard to those that can be described in terms of binding of electrons and holes within the region of the graphene spectrum dominated by the linear dispersion of the Dirac cones.

Here we present a theory and experimental observations of the interaction of excitons composed of Dirac fermions confined in triangular colloidal graphene quantum dots (GQDs).[13,29−31] In these dots valley degeneracy translates into degeneracy of conduction and valence band edges[13,30] and existence of orbitally bright and dark exciton states.[13] We observe interband transitions from the lowest orbitally dark singlet exciton states to a bound two-electron−two-hole state (biexciton) that can be described in terms of a dark exciton and bright exciton bound by ∼0.14 eV. While this binding is 1 order of magnitude less than the gap, it is strong compared to biexciton binding in semiconductor quantum dots[1,32,33] and carbon nanotubes.[2,34] The importance of strong Coulombic interactions in multiple exciton generation in solar cells,[35]

photon cascades,[36] and other applications suggest that such new technologies may be realized using GQDs.

Quasi-electrons and quasi-holes in finite size graphene, graphene quantum dots (GQDs), can be understood in terms of confined Dirac fermions.[12,29,37] In particular, scaling of the optical gap with the size of the quantum dot from nanometer to submicron agrees very well with that of confined Dirac Fermion electrons and holes.[29] The inset in Figure 1 shows the states at
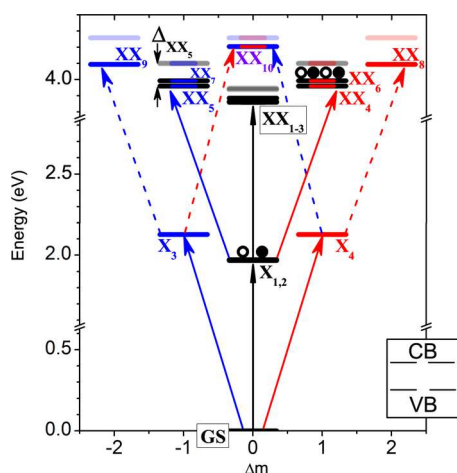
Figure 1. Extrapolated singlet exciton (X) and biexciton (XX) states, relative to the ground state (GS), of confined Dirac fermions derived from the two-fold orbitally degenerate HOMO and LUMO states illustrated in the inset. Biexciton states are colored according to the single-exciton states that make the dominant contributions to the corresponding biexciton. Partially transparent horizontal lines indicate the biexciton states in the case of zero biexciton binding energy. As an example, the binding energy for biexciton state XX_5 is shown by Δ_{XX_5}. Dipole-allowed interband electronic transitions, corresponding to $\Delta m = \pm 1$, are labeled with arrows. $\Delta m = +1$ corresponds to σ^+ photon polarization (red arrow), and $\Delta m = -1$ corresponds to σ^- photon polarization (blue arrow). The transitions relevant to transient-absorption measurements at long delays, when only the ground and the nominally dark singlet exciton states $X_{1,2}$ are populated, are indicated by solid arrows. Black arrows represent orbitally forbidden transitions that become allowed due to electron-phonon coupling. Filled circles represent conduction-band electrons, and open circles represent (valence-band) holes.

the top of the valence and bottom of the conduction band in colloidal graphene quantum dots[13,30] with the atomic structure shown as an inset in Figure 2a. The GQDs (labeled C168) have double-armchair edges and exactly 168 carbon atoms in the sp^2-hybridized core.[11] Confinement opens a gap of $E_g \sim 1.6$ eV. The ligands shown in black serve to cage the GQDs and thereby inhibit their aggregation and promote solubility, but they have negligible influence on the electronic structure of the GQD core as steric hindrance forces the phenyl groups to rotate out of the plane of the core.[11,38] The gap can be understood in terms of a tight-binding model yielding Dirac cones for bulk graphene[13] or for armchair edges and larger structures directly from a confined Dirac Fermion model.[12] The three-fold rotational symmetry of C168 allows us to label the electronic states with quantum numbers $m = 0, 1,$ and 2 with optically bright transitions occurring only between states for which $\Delta m = \pm 1$, as demonstrated by both tight-binding and ab initio calculations[13] and illustrated in Figure 1. The singlet exciton spectrum, shown at the bottom of Figure 1, consists of two bright, $\Delta m = \pm 1$ (X_3, X_4), and two orbitally dark, $\Delta m = 0$
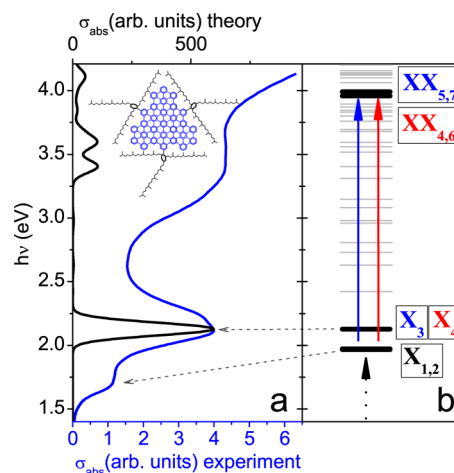
Figure 2. (a) Experimental (blue) and theoretical (black) absorption cross section of C168. Inset shows the molecular structure of C168, with the GQD core in blue and ligands in black. (b) Calculated singlet exciton (X) and biexciton states (XX). Gray lines show higher-energy single-exciton states obtained by either dipole-allowed excitation from the ground state or by one of the carriers excited from $X_{1,2}$. The XX states are the biexciton states accessible by absorption of a photon from $X_{1,2}$.

(X_1, X_2), excitons. The energy of triplet excitons, discussed in ref 13, falls close to the energy of the two orbitally dark singlet excitons resulting in the bright-singlet−triplet splitting energy being close to the energy difference between the $X_{1,2}$ and $X_{3,4}$ excitons. Because of the degeneracy of the HOMO and LUMO levels, there exist different classes of biexciton (XX) states consisting largely of pairwise combinations of single-exciton states as illustrated in Figure 1.

The exciton states give rise to the calculated and measured absorption spectra shown in Figure 2a. Although $X_{1,2}$ (or collectively LX) are orbitally optically dark,[13,30,31] their coupling to phonons allows for borrowing of oscillator strength from higher-energy bright excitons thereby producing the absorption shoulder at 1.7 eV.[39] The pronounced peak at 2.1 eV is associated with $X_{3,4}$. Figure 2b shows excited singlet exciton states obtained by either dipole-allowed excitation from the ground state or by excitation of one of the carriers from the states $X_{1,2}$. The XX states studied here experimentally are the biexcitons accessible by optical absorption from $X_{1,2}$.

Measurement of biexciton emission in C168 is extremely challenging on account of the low photoluminescence quantum yield of C168 single excitons ($\sim$0.002) and rapid rate (3 ps^{-1}) of biexciton Auger recombination.[31] Moreover, rapid carrier cooling allows for measurement of photoluminescence only from the lowest-energy single- and biexciton states. Therefore, we study biexcitons by transient absorption (TA) measurements in which the single-to-biexciton transition does not require a long-lived biexciton for its observation and in which one can access higher-energy biexcitons. TA measurements on C168 were performed as described previously.[31] C168 was prepared following the synthesis of Yan and Li.[11] Prior characterization has established the high structural and size uniformity of the synthetic product.[11] C168 was dissolved in anhydrous toluene, and loaded in a nitrogen atmosphere in a 1 mm path length fused-silica cuvette sealed with Teflon valves. GQD solutions were prepared to optical densities of $\sim$0.2 at 3.1 eV. C168 in toluene was excited at 3.1 eV and probed with $\sim$130 fs temporal resolution using a broadband continuum (for

photon energies $\hbar\omega_{probe} \geq 1.1$ eV) or the output of a β-BaB$_2$O$_4$-based optical parametric amplifier (for 0.5 eV $\leq \hbar\omega_{probe} < 1.05$ eV). Spectra above 1.1 eV were measured with a charge-coupled-device (CCD) spectrometer and below 1.1 eV with a monochromator and InGaAs photodiode. In each case, the spectral resolution was 2 nm. To account for the solvent response, identical measurements were performed on a cuvette filled with toluene alone, the response of which was subtracted from the data for C168 in solution.

Excitation of C168 at 3.1 eV with a pump fluence of 0.8 mJ cm^{-2} per pulse yields the TA spectrum of Figure 3. The
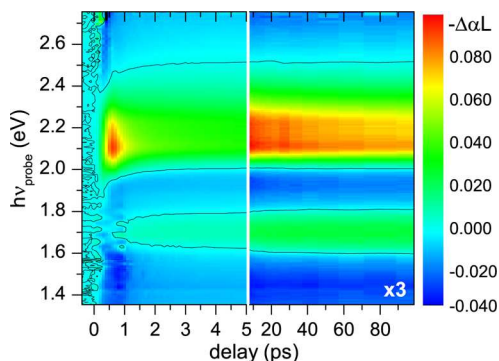
Figure 3. Transient absorption spectrum showing $-\Delta\alpha L$ as a function of probe photon energy and delay for C168 excited at 3.1 eV at a fluence of 0.8 mJ cm^{-2} per pulse (1.6×10^{15} photons cm^{-2} per pulse). The color scale corresponds to the data at delays $t \leq 5.0$ ps. The data at $t > 8$ ps are multiplied by 3 to match scales. The black curves indicate the contours for $\Delta\alpha L = 0$.

effective absorption cross section of the GQDs at 3.1 eV is $\sigma_0 \sim 6 \times 10^{-15}$ cm^2 so that the optical response is saturated[31] and essentially all the GQDs are initially excited with at least two excitons. Resolution-limited carrier cooling is followed by biexciton Auger recombination on a 0.3 ps time scale and then lattice cooling over tens of picoseconds.[31] We focus on long delays (100 ps), when the system has cooled to the lowest-energy singlet exciton states $X_{1,2}$. The probe then measures transitions from $X_{1,2}$ to higher-energy single-exciton (X*) and XX states. The spectral shape is unchanged for times of at least 1 ns. Bleaches of the ground-state transitions ($\sim$1.7 and 2.1 eV) are accompanied by induced absorption ($-\Delta\alpha L < 0$) immediately to the red ($\sim$1.45 and 1.95 eV). Such patterns are characteristic of biexciton binding;[1] population of $X_{1,2}$ opens new transitions $X_{1,2} \rightarrow XX_{X_{1,2}+X_n}$ (the subscript for XX here denotes the single-exciton states of which the biexciton is primarily composed), which require less energy than the $0 \rightarrow X_n$ transition because of the bound nature of the final state.

For a theoretical understanding of the TA spectrum, we performed microscopic calculations of the absorption spectrum of photoexcited C168 including the low-energy exciton and biexciton states via a combination of tight-binding (tb), Hartree–Fock (HF), and configuration interaction (CI) methods.[13] The many-body Hamiltonian of the GQD describes interacting electrons in p$_z$ carbon orbitals. With the electron creation operators for a p$_z$ orbital with spin σ on atom i denoted by $c_{i,\sigma}^+$, the Hamiltonian for N carbon atoms with N electrons reads

$$\hat{H} = \sum_{i,l=1}^{N}\sum_{\sigma} \tau_{il} c_i^+ c_l + \frac{1}{2}\sum_{i,j,k,l}\sum_{\sigma,\sigma'} \langle ij|V|kl\rangle c_{i,\sigma}^+ c_{j,\sigma'}^+ c_{k,\sigma'} c_{l,\sigma}$$

(1)

The first term is the one-electron tight-binding Hamiltonian, and the second term, $\langle ij|V|kl\rangle$, describes the screened electron–electron interactions, $V(\vec{r} - \vec{r}') = 2/(\kappa|r - r'|)$.[13] Screening by sigma electrons and the surrounding fluid is included through the dielectric constant κ. We next perform Hartree–Fock calculations, which rotate the $c_{i,\sigma}^+$ site operators into HF operators $b_{j,\sigma}^+$, where j labels the HF states. The ground and excited states of the GQD are expanded in multipair excitations of Dirac fermions out of the HF ground state $|0\rangle$

$$|\nu\rangle = k_0^{\nu}|0\rangle + \sum_{i,j,\sigma} k_{ij}^{\nu(1)} b_{i\sigma}^+ b_{j\sigma} |0\rangle$$
$$+ \sum_{i,j,k,l}\sum_{\sigma_1,\sigma_2} k_{ijkl}^{\nu(2)} b_{i\sigma_1}^+ b_{j\sigma_2}^+ b_{k\sigma_1} b_{l\sigma_2} |0\rangle + ...$$

The CI Hamiltonian matrix is built in the space of multipair excitations and diagonalized numerically. To capture Auger coupling in CI calculations, we keep HF states within an energy window of $3E_g$. The tunneling matrix elements in eq 1 are $\tau = -4.2$ eV for nearest neighbors and $\tau' = -0.1$ eV for next-nearest neighbors, which are chosen to give bright singlet excitons at 2.128 eV, close to the strong absorption peak measured at 2.1 eV while the dielectric constant, which determines the bright-singlet–dark-triplet splitting, was chosen as $\kappa = 5$, similar to the expected value for extended graphene in toluene,[21] to reflect screening by sigma electrons and surrounding fluid.

For interpreting the experimental data at long delays, we focus on the band-edge XXs. The calculated singlet excitons and biexcitons derived from the degenerate HOMO + LUMO band-edge HF states are shown in Figure 1. These XX states can be classified according to whether the single-exciton states from which they are primarily derived include two, one, or zero $X_{1,2}$ excitons and are labeled respectively as XX_{1-3}, XX_{4-7}, and XX_{8-10}. Combined with the $\Delta m = \pm 1$ selection rule, this determines the allowed transitions (solid blue and red arrows) in Figure 1. Biexciton binding energies are defined as $\Delta_{XX_i} = (E_{X_j} + E_{X_k}) - E_{XX_i}$, where X_j and X_k are the single-exciton states primarily constituting XX_i. We calculate $\Delta_{XX_{1-3}} = 56$–82 meV, $\Delta_{XX_{4,5}} = 142$ meV, and $\Delta_{XX_{6,7}} = 104$ meV. Also shown in Figure 2b by gray lines are all higher-energy singlet excitons (X*) that are accessible from $X_{1,2}$.

Data for $t = 100$ ps in Figure 3 are plotted as blue circles in Figure 4a, which includes additional low-energy data. For quantitative determination of the experimental biexciton binding energy, we model the TA spectrum as follows. The energies of the ground-state optical transitions are determined by the positions of the peaks of $-[(d^2\alpha_0)/(d\omega^2)]$,[40] which yields two features in the low-energy shoulder, one at 1.68 eV and a smaller one at 1.86 eV, corresponding to $X_{1,2}$, which is optically brightened by coupling through phonons to higher-energy bright excitons;[39] two in the peak around 2.1 eV, one at 2.09 eV and another of about half the amplitude at 2.22 eV, corresponding to $X_{3,4}$; and another around 2.6 eV, corresponding to excitons derived from other than a band-edge electron–hole pair. The spectral widths of the $X_i \rightarrow X_i + X_j$ and $0 \rightarrow X_j$ transitions are set as equal because the main source of additional line broadening for transitions to biexciton states is
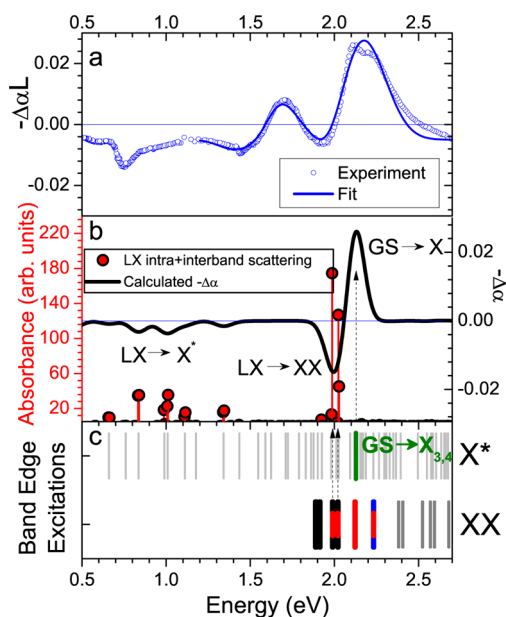
Figure 4. Plot of experimental and theoretical absorption spectra from the lowest singlet exciton state. (a) The blue circles indicate measured $-\Delta\alpha L(\hbar\omega, t = 100 \text{ ps})$ for C168. The blue curve is a fit (see main text) to the experimental data. (b) The red bars indicate calculated transitions from the states $X_{1,2}$ accounting for intra+interband transitions. The black line is the Gaussian-broadened (50 meV) $-\Delta\alpha = -(\alpha_{1,2} - \alpha_0)$ calculated from the microscopic theory assuming equally populated $X_{1,2}$ states. (c) The lower panel shows singlet excitons (light gray), band-edge excitons (color corresponding to Figure 1) and higher XXs (dark gray) accessible from $X_{1,2}$.

expected to be Auger recombination, which leads to a biexciton lifetime of $\tau_{XX} = 0.3$ ps.[31] This corresponds to broadening 1 order of magnitude less than the widths of the features observed in ground-state absorption. We label by Δ_i the biexciton binding energy of the biexciton formed from addition of an exciton X_i to the lowest-energy singlet exciton. To minimize the number of free parameters, we set $\Delta_1 = \Delta_2$ and $\Delta_3 = \Delta_4$. This is summarized by the function $-\Delta\alpha(\hbar\omega)L = \delta\alpha L + \sum_{i=1}^{4} \beta_{X_i}[g_{X_i}(\hbar\omega) - R_i\, g_{X_i}(\hbar\omega + \Delta_i)]$, where $\delta\alpha L$ is a spectrally flat induced absorption taken as -0.005 to account for the broad induced absorption; $g_{X_i}(\hbar\omega)$ are normalized Gaussians taken from the fit to the ground-state absorption spectrum; and R_i is the ratio of the strength of the $X_1 \rightarrow X_1 + X_i$ transition to the strength of the $0 \rightarrow X_i$ transition. We assume that $\beta_1 = \beta_2$ and $\beta_3 = \beta_4$. Our fitting parameters are then $\Delta_{1,3}$, $\beta_{1,3}$, and $R_{1,3}$. On the basis of the effects of state-filling in a single-particle picture, we expect $R_3 = 1/2$. As discussed below, calculations indicate that the absorption on transitions $X_1 \rightarrow XX_{6,7}$ and $X_2 \rightarrow XX_{4,5}$ are 0.43 to 0.59 times the absorption on the transition from the ground state to $X_{3,4}$. Hence, we constrain R_3 to the range from 0.43 to 0.59.

A best fit of the TA spectrum in the range from 1.1 to 2.6 eV using the above model is shown by the solid blue curve in Figure 4 with $\Delta_1 = 0.28 \pm 0.03$ eV and $\Delta_3 = 0.14 \pm 0.01$ eV. The fit yields $R_1 = 0.22 \pm 0.01$ and $R_3 = 0.59 \pm 0.01$. However, induced absorption features at 0.6 and 0.75 eV suggest that we must consider the possibility of intraband contributions to the TA spectrum in the 1.3 to 2.5 eV region.

To confirm the origin of the spectral features in the experimental TA spectrum shown in Figure 4a, we use the microscopic model described earlier to calculate the TA

spectrum $-(\alpha_{LX}(\hbar\omega) - \alpha_0(\hbar\omega))$ shown by the black curve in Figure 4b. The TA curve involves bleaching of optical transitions from the ground state, particularly the transition GS $\rightarrow X_{3,4}$ to the bright excitons shown in green in Figure 4c. This gives rise to the peak in TA at 2.1 eV. The TA spectrum also involves optical transitions from a photoexcited state to excited exciton, X*, and biexciton, XX, states shown in Figure 4c and yielding $-\alpha_{LX}(\hbar\omega)$. In particular, the dip at 1.95 eV is due to $X_1 \rightarrow XX_{6,7}$ and $X_2 \rightarrow XX_{4,5}$ transitions that involve addition of a bright $X_{3,4}$ exciton to the photoexcited LX. This supports the interpretation of the experimental feature at this energy being due to a biexciton bound by 0.14 eV. The relative strengths of the $X_1 \rightarrow XX_{6,7}$ and $X_2 \rightarrow XX_{4,5}$ transitions are respectively 0.43 and 0.59 times the GS $\rightarrow X_{3,4}$ transition, which is on average in agreement with the simple expectation of 1/2 from counting arguments. Figure 4a,b shows negative TA contributions at energies $E < 1.5$ eV, well below the XX transitions, due to intraband excitations of photoexcited electrons and holes from LX to exciton states X* derived primarily from single-particle states other than the HOMO or LUMO. While the calculated and measured energy ranges of the X* contribution are in excellent agreement, the broadening of the experimental spectra prevents detailed comparison of energies of excited exciton states X*. The positive contribution in experiment, Figure 4a, at 1.7 eV corresponds to both interband transitions to dark exciton states that are prohibited in the calculated spectra, which do not account for electron–phonon coupling, and to intraband transitions around 1.3 eV. This makes definitive determination of Δ_{1-3} from the experimental data challenging.

These experiments and theory demonstrate the nontrivial interaction of excitons composed of Dirac fermions confined in graphene quantum dots. Despite predictions of strong exciton–exciton interactions potentially leading to excitonic instabilities, we find that the biexciton binding energy is 1 order of magnitude less than the optical gap but stronger than in semiconductor quantum dots[1,32,33] and carbon nanotubes.[2] The observation of such large biexciton binding in a structure only about 2 nm across may be surprising. In colloidal CdSe quantum dots, biexciton binding increases with decreasing dot radius until a radius $\lesssim$1.8 nm (substantially larger than the size of C168) at which point the trend reverses[41] on account of the balance between confinement and Coulomb interactions. In a system with parabolic band structure, the confinement energy scales with nanocrystal size L as L^{-2}, whereas the Coulomb interaction scales as L^{-1}. At sufficiently small size, confinement dominates the Coulomb interaction to a degree that the latter cannot produce sufficient deformation of the wave function of the four-particle relative motion to produce continuing growth in the biexciton binding.[42] However, in the size regime where the low-energy electronic structure of GQDs can be described in terms of confined Dirac fermions, that is, for a linearly dispersive band structure, the confinement energy only scales as L^{-1} so that Coulomb interactions grow in step with confinement. Our conclusions are drawn for Coulomb interactions screened by surrounding fluid; future work will investigate the effect of size and microscopic screening on exciton–exciton interactions.

Determination of the binding of biexciton states characteristic of the degenerate HOMO and LUMO levels of graphene quantum dots has several implications for the photophysics of GQDs. For example, efficient multiple-exciton generation (MEG) is dependent on strong Coulomb interactions and relaxed momentum-conservation constraints that allow gen-

eration of multiple carriers to occur before excess carrier energy is lost.[43,44] These are reflected respectively in the biexciton binding energy observed here and the fast Auger recombination reported previously.[31] Extended graphene has been found to display high rates of MEG at low excitation fluences.[45] While that may be useful in photodetectors, it is of limited utility for photovoltaic solar cells, where one desires a band gap of $\gtrsim 1.0$ eV, as can be generated in GQDs. The possibility of efficient MEG in graphene nanostructures has been seen in computations,[46] while semiconducting single-walled carbon nanotubes have already been found to display surprisingly efficient impact ionization.[7,47] The rapid extraction of carriers from GQDs, as reported for GQDs anchored to $TiO_2(110)$,[48] would be an essential step in overcoming rapid Auger recombination and making use of any excess carriers generated by MEG.

■ AUTHOR INFORMATION

Corresponding Authors
*E-mail: pawel.hawrylak@uottawa.ca.
*E-mail: mcguire@pa.msu.edu.

Notes
The authors declare no competing financial interest.

■ ACKNOWLEDGMENTS

■ REFERENCES

(1) Hu, Y. Z.; Koch, S. W.; Lindberg, M.; Peyghambarian, N.; Pollock, E. L.; Abraham, F. F. *Phys. Rev. Lett.* **1990**, *64*, 1805.

(2) Colombier, L.; Selles, J.; Rousseau, E.; Lauret, J. S.; Vialla, F.; Voisin, C.; Cassabois, G. *Phys. Rev. Lett.* **2012**, *109*, 197402.

(3) Klimov, V. I.; Mikhailovsky, A. A.; McBranch, D. W.; Leatherdale, C. A.; Bawendi, M. G. *Science* **2000**, *287*, 1011.

(4) Wang, F.; Dukovic, G.; Knoesel, E.; Brus, L. E.; Heinz, T. F. *Phys. Rev. B: Condens. Matter Mater. Phys.* **2004**, *70*, 241403.

(5) Huang, L. B.; Krauss, T. D. *Phys. Rev. Lett.* **2006**, *96*, 057407.

(6) Schaller, R. D.; Klimov, V. I. *Phys. Rev. Lett.* **2004**, *92*, 186601.

(7) Gabor, N. M.; Zhong, Z. H.; Bosnick, K.; Park, J.; McEuen, P. L. *Science* **2009**, *325*, 1367.

(8) Wang, F.; Wu, Y.; Hybertsen, M. S.; Heinz, T. F. *Phys. Rev. B: Condens. Matter Mater. Phys.* **2006**, *73*, 245424.

(9) Robel, I.; Gresback, R.; Kortshagen, U.; Schaller, R. D.; Klimov, V. I. *Phys. Rev. Lett.* **2009**, *102*, 177404.

(10) Muller, M.; Kubel, C.; Mullen, K. *Chem. - Eur. J.* **1998**, *4*, 2099.

(11) Yan, X.; Cui, X.; Li, L. S. *J. Am. Chem. Soc.* **2010**, *132*, 5944.

(12) Rozhkov, A. V.; Nori, F. *Phys. Rev. B: Condens. Matter Mater. Phys.* **2010**, *81*, 155401.

(13) Ozfidan, I.; Korkusinski, M.; Guclu, A. D.; McGuire, J. A.; Hawrylak, P. *Phys. Rev. B: Condens. Matter Mater. Phys.* **2014**, *89*, 085310.

(14) Castro Neto, A. H.; Guinea, F.; Peres, N. M. R.; Novoselov, K. S.; Geim, A. K. *Rev. Mod. Phys.* **2009**, *81*, 109.

(15) Kotov, V. N.; Uchoa, B.; Pereira, V. M.; Guinea, F.; Castro Neto, A. H. *Rev. Mod. Phys.* **2012**, *84*, 1067.

(16) Hofmann, J.; Barnes, E.; das Sarma, S. *Phys. Rev. Lett.* **2014**, *113*, 105502.

(17) Faugeras, C.; Berciaud, S.; Leszczynski, P.; Henni, Y.; Nogajewski, K.; Orlita, M.; Taniguchi, T.; Watanabe, K.; Forsythe, C.; Kim, P.; Jalil, R.; Geim, A. K.; Basko, D. M.; Potemski, M. *Phys. Rev. Lett.* **2015**, *114*, 126804.

(18) Li, Z. Q.; Henriksen, E. A.; Jiang, Z.; Hao, Z.; Martin, M. C.; Kim, P.; Stormer, H. L.; Basov, D. N. *Nat. Phys.* **2008**, *4*, 532.

(19) Bostwick, A.; Speck, F.; Seyller, T.; Horn, K.; Polini, M.; Asgari, R.; MacDonald, A. H.; Rotenberg, E. *Science* **2010**, *328*, 999.

(20) Mak, K. F.; da Jornada, F. H.; He, K. L.; Deslippe, J.; Petrone, N.; Hone, J.; Shan, J.; Louie, S. G.; Heinz, T. F. *Phys. Rev. Lett.* **2014**, *112*, 207401.

(21) Elias, D. C.; Gorbachev, R. V.; Mayorov, A. S.; Morozov, S. V.; Zhukov, A. A.; Blake, P.; Ponomarenko, L. A.; Grigorieva, I. V.; Novoselov, K. S.; Guinea, F.; Geim, A. K. *Nat. Phys.* **2011**, *7*, 701.

(22) Hwang, C.; Siegel, D. A.; Mo, S. K.; Regan, W.; Ismach, A.; Zhang, Y. G.; Zettl, A.; Lanzara, A. *Sci. Rep.* **2012**, *2*, 590.

(23) Khveshchenko, D. V. *Phys. Rev. Lett.* **2001**, *87*, 246802.

(24) Drut, J. E.; Lahde, T. A. *Phys. Rev. Lett.* **2009**, *102*, 026802.

(25) Stroucken, T.; Grönqvist, J. H.; Koch, S. W. *Phys. Rev. B: Condens. Matter Mater. Phys.* **2011**, *84*, 205445.

(26) Paananen, T.; Egger, R. *Phys. Rev. B: Condens. Matter Mater. Phys.* **2011**, *84*, 155456.

(27) Sorella, S.; Otsuka, Y.; Yunoki, S. *Sci. Rep.* **2012**, *2*, 992.

(28) Denk, R.; Hohage, M.; Zeppenfeld, P.; Cai, J. M.; Pignedoli, C. A.; Sode, H.; Fasel, R.; Feng, X. L.; Mullen, K.; Wang, S. D.; Prezzi, D.; Ferretti, A.; Ruini, A.; Molinari, E.; Ruffieux, P. *Nat. Commun.* **2014**, *5*, 4253.

(29) Guclu, A. D.; Potasz, P.; Korkusinski, M.; Hawrylak, P. *Graphene Quantum Dots*; Springer Verlag: Berlin, 2014.

(30) Schumacher, S. *Phys. Rev. B: Condens. Matter Mater. Phys.* **2011**, *83*, 081417.

(31) Sun, C.; Figge, F.; McGuire, J. A.; Li, Q. Q.; Li, L. S. *Phys. Rev. Lett.* **2014**, *113*, 107401.

(32) Masumoto, Y.; Okamoto, S.; Katayanagi, S. *Phys. Rev. B: Condens. Matter Mater. Phys.* **1994**, *50*, 18658.

(33) Hawrylak, P.; Korkusinski, M. In *Single Quantum Dots: Fundamentals, Applications and New Concepts*; Micheler, P., Ed.; Topics in Applied Physics; Springer-Verlag Berlin: Berlin, 2003; Vol. 90; p 25.

(34) Yuma, B.; Berciaud, S.; Besbas, J.; Shaver, J.; Santos, S.; Ghosh, S.; Weisman, R. B.; Cognet, L.; Gallart, M.; Ziegler, M.; Honerlage, B.; Lounis, B.; Gilliot, P. *Phys. Rev. B: Condens. Matter Mater. Phys.* **2013**, *87*, 205412.

(35) Semonin, O. E.; Luther, J. M.; Choi, S.; Chen, H. Y.; Gao, J. B.; Nozik, A. J.; Beard, M. C. *Science* **2011**, *334*, 1530.

(36) Benson, O.; Santori, C.; Pelton, M.; Yamamoto, Y. *Phys. Rev. Lett.* **2000**, *84*, 2513.

(37) Zhang, Z. Z.; Chang, K.; Peeters, F. *Phys. Rev. B: Condens. Matter Mater. Phys.* **2008**, *77*, 235411.

(38) Yan, X.; Cui, X.; Li, B. S.; Li, L. S. *Nano Lett.* **2010**, *10*, 1869.

(39) Riesen, H.; Wiebeler, C.; Schumacher, S. *J. Phys. Chem. A* **2014**, *118*, 5189.

(40) Martin, A. E. *Nature* **1957**, *180*, 231.

(41) Achermann, M.; Hollingsworth, J. A.; Klimov, V. I. *Phys. Rev. B: Condens. Matter Mater. Phys.* **2003**, *68*, 245302.

(42) Takagahara, T. *Phys. Rev. B: Condens. Matter Mater. Phys.* **1989**, *39*, 10206.

(43) Franceschetti, A.; An, J. M.; Zunger, A. *Nano Lett.* **2006**, *6*, 2191.

(44) Allan, G.; Delerue, C. *Phys. Rev. B: Condens. Matter Mater. Phys.* **2008**, *77*, 125340.

(45) Plotzing, T.; Winzer, T.; Malic, E.; Neumaier, D.; Knorr, A.; Kurz, H. *Nano Lett.* **2014**, *14*, 5371.

(46) McClain, J.; Schrier, J. J. *J. Phys. Chem. C* **2010**, *114*, 14332.

(47) Wang, S. J.; Khafizov, M.; Tu, X. M.; Zheng, M.; Krauss, T. D. *Nano Lett.* **2010**, *10*, 2381.

(48) Williams, K. J.; Nelson, C. A.; Yan, X.; Li, L. S.; Zhu, X. Y. *ACS Nano* **2013**, *7*, 1388.